Towards large scale orientation mapping using the eCHORD method

Clément Lafond, Thierry Douillard, S. Cazottes, M. De Graef, P. Steyer, Cyril Langlois

Towards large scale orientation mapping using the eCHORD method

C. Lafond[1*], T. Douillard[1], S. Cazottes[1], M. De Graef[2], P. Steyer[1], C. Langlois[1]

[1] Université de Lyon, INSA-Lyon, MATEIS CNRS UMR5510, 7 avenue Jean Capelle, 69621 Villeurbanne (France)

[2] Department of Materials Science and Engineering, Carnegie Mellon University, Pittsburgh USA

* corresponding author

Keywords: Orientation mapping, SEM, Electron Channeling, EBSD, Large area mapping

Highlights:

- A procedure to correct the effect of the electron beam scanning when using the eCHORD approach is proposed
- The procedure is based on a rotation matrix applied on each pixel of the map.
- It paves the way for centimetric orientation mapping in texture studies and geological studies

Abstract

eCHORD is an alternative method for orientation mapping in Scanning Electron Microscopy that involves channeling contrast observed in BSE images. The sample tilt being small (10°), eCHORD could be a promising method for large scale maps as it limits the image deformation sometimes observed with EBSD maps. However, when the magnification is low, the scan deflection of the beam becomes important, which may modify the channeling conditions of analyzed grains, leading to orientation errors. A correction method for the resulting orientations is proposed and a resulting map on a Si single crystal is presented with an experimental misorientation of 0.12° across a field of view of 2.3x1.7mm^2.

1. Introduction

Orientation mapping brings crucial information to study the relationship between microstructure and properties in crystalline materials. For the study of textured materials, or large grain sized materials, large orientation maps are required. Particularly, mapping the orientations on large fields can be necessary, for instance when the texture of the material varies spatially on a large scale, or when the grain size is in the millimetric/centimetric range. This is the case for Al alloy [1,2], or geological materials [3,4]. In scanning electron microscopy (SEM), one of the conventional tools to obtain orientation maps is the Electron Back-Scattered Diffraction (EBSD) technique. Some experimental limitations are associated to the use of EBSD for large scale orientation mapping. The EBSD acquisition geometry is intrinsically a limit (70° tilt of the sample and short distance between the sample and the detector). Also, the large sample tilt leads also to anisotropy of the spatial resolution between lateral and transverse directions. The scan distortions are difficult to correct and complicate any comparison between different imaging modalities (EBSD and EDS mapping, BSE imaging)[5,6]. Mapping large areas using a sample tilted to 70° is also problematic because of the risk of the sample touching the SEM objective lens. It is the case when studying, for example, geological samples, for which the size of the grains can be in the centimeter range [7].

Another orientation mapping approach in a SEM has been proposed recently, exploiting the channeling contrast of the Back Scattered Electron (BSE) signal, and relying on a simpler acquisition geometry [8]. This method, called **eCHORD**, is based on the acquisition of multiple electron channeling contrast images acquired during a rotation of a tilted sample. From an image

series, intensity profiles are extracted on each position of the region of interest (ROI) and then compared to a theoretical database to retrieve the crystal orientations [9–11]. One of the advantages of eCHORD is that it requires a low sample tilt (typically 10°). Therefore, it may allow large fields of view mapping at the centimetric scale on large size samples. However, eCHORD is based on the channeling contrast evolution, which is directly dependent on the beam direction relative to the sample. To open eCHORD to large area mapping, it is necessary to well understand the influence of the beam scanning the surface, among other issues linked to the work at low magnification and particularly the spatial distortions due to the lens aberrations. Actually, to form the SEM image, the incident beam is deflected from the original incident beam direction, initially positioned at the center of the field of view. The effect of the beam scanning on the channeling phenomenon is particularly evidenced at low magnification (i.e., a large field of view) where Kikuchi bands are visible on a monocrystalline sample or even on a polycrystalline sample with large grain size [12]. This would have an impact on the angular precision of the eCHORD indexation results because, up to now, the eCHORD theoretical background makes the assumption that the angle between the electron beam and the rotation axis is always equal to the sample tilt, without considering the extra deflection of the beam when it scans the surface [8].

This problem is also present in EBSD. When scanning the surface of the sample, the beam deflection changes the pattern center on the Kikuchi pattern, and thus the orientations found are misoriented from the expected orientations. After calibration, the pattern center position is corrected depending on the deviation of the beam to obtain a more precise orientation [13]. A recent approach using pattern-matching refinement of the pattern center leads to a

misorientation error of only 0.09° across a field of view of 1mm [14]. In the eCHORD framework, understanding and correcting the effect of the beam deflection is a prerequisite in order to obtain reliable large orientation maps.

In the present study, the eCHORD experimental set-up is first presented. Then, the geometry of acquisition is detailed in order to describe the beam deflection variation during the rotation of the tilted sample. In the following section, experimental intensity profiles extracted from a low magnification image series acquired on a Si single crystal are analyzed to determine the influence of the beam deflection during the scan. The procedure to correct for the scan influence is then presented, followed by a discussion.

2. Experimental Set-Up

All the experiments have been carried out on a silicon single crystal cut along a {001} plane. Image series were acquired on a Gemini I SEM (Carl Zeiss Microscopy GmbH, Oberkochen, Germany) operating at an acceleration voltage of 15kV, with an aperture size of 60μm and with the high current mode activated. A working distance of 7mm was used. A retractable standard 4 Quadrant solid-state detector (namely 4Q-BSD) placed at the bottom of the objective lens was used. These parameters have been chosen in order to be identical to those used in the reference paper [8]. The high current mode is active as it reduces the beam divergence while increasing the signal on the BSE detector. The working distance has been set to 7 mm to collect a maximum of BSE on the detector. The 15kV with a 10° sample tilt allows obtaining detailed experimental profiles, which are easily indexable. A rotation from 0° to 360° was performed with a sample tilt

of 10° and a rotation step of 2°. The full rotation was done automatically with the sample placed on a piezo-controlled precision sub-stage (SmarAct GmbH, Germany) mounted on the top of the microscope goniometer allowing a precision of 1 micro-degree in rotation. The sub-stage has three degrees of freedom: two translations situated on top of a rotation. The sample is fixed on the translation part. Before the rotation, two operations have been performed: 1/ the axis of rotation of the substage has been set to coincide with the electron column optical axis by moving the substage using the X and Y translations of the SEM stage goniometer, and 2/ the sample ROI has been centered in the field of view using the X and Y translations of the substage. The scan deflection, then, has been deliberately maximized by choosing the largest field of view. A field of view of 2.3x1.7 mm^2 was scanned (magnification x50) with a pixel size of 4.49μm and image size equal to 512x384 pixels. Using a time per frame of 2.6 seconds, a full image series of 180 images was acquired in approximately 8 minutes. At each step of the rotation, the scanned area is automatically rotated to follow the rotation of the sample. As a consequence, the details in the image remain in the same orientation in the field of view during the rotation of the sample while the channeling contrast is varying. It is worth noting that the dedicated SmarAct stage is very convenient for the acquisition, but not strictly necessary. Particularly, if the rotation part of the built-in microscope goniometer is located under the translation part, the same procedure as the one described above can be used. In the case of a translation part located under the rotation part, three possibilities must be considered: 1/ a manual acquisition where at each rotation step the ROI is manually re-centered at the original position; 2/ a precise compucentric mode is available on the microscope and could be used to re-center the ROI automatically at each rotation step; 3/ the center of rotation of the goniometers could be placed in coincidence with the electron beam

optical axis using built-in X and Y translations, but in this case the only region that can be mapped is the one on top of the rotation axis.

An image denoising step using the VSNR algorithm [15] has been applied with a Dirac filter of parameters sigma 0.15 and 30 iterations.

3. Details about acquisition geometry

As electron channeling is highly dependent on the beam direction relative to the crystal, the most probable impact on the images would be due to the incident angle of the beam across the region of interest. The beam is controlled by deflectors located in the SEM column [16] that modify the electron beam direction using a pivot point located above the objective lens. The incident beam is then deviated from the original normal incidence to scan every (x,y) position of the ROI.

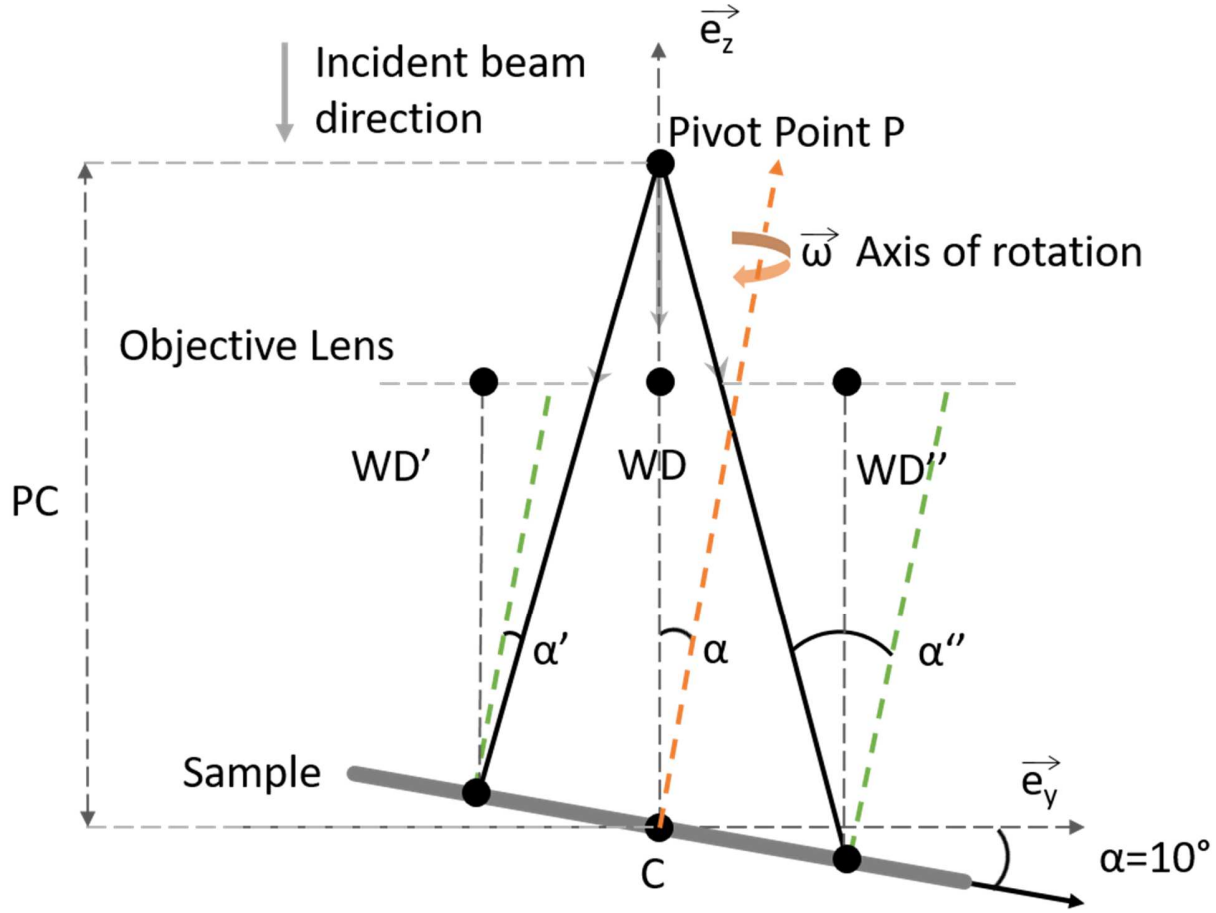

Figure 1: Geometry of acquisition. The sample is tilted to an angle α of 10° around $\vec{e}_x$ and rotated around the axis of rotation $\vec{\omega}$. The incident beam is deflected from the pivot point P during the scan of the field of view. The angle between the electron beam and the local normal to the surface, as well as the working distance WD vary differently for each scanned point during the rotation. PC is the distance between pivot point P and C, the center of ROI.

Fig 1 represents the experimental setup for a sample tilted by an angle α relative to the $\vec{e}_x$ axis and with a rotation of angle ω_i around the axis of rotation $\vec{\omega}$ (i.e. the normal of sample surface). PC is the distance between the pivot point and the center of the field of view.

Each scanned point is located at a coordinate (X, Y) from the center defined as $(x-x_c, y-y_c)$, with (x_c, y_c) the coordinates of the center. At the center of the field of view, the incident beam is traveling in the opposite direction of the axis $\vec{e}_z$. Considering that the position of the point C at the center remains unchanged during the rotation, the angle between the incident beam and the sample normal as well as the working distance, are constant for point C. This is the perfect case for which the experimental eCHORD profile can be described by a perfect circular path in the corresponding Electron Channeling Pattern (ECP) with α the radius of the circle [8]. For all other positions, the angle between the beam direction and the local sample normal as well as the working distance are a function of $(\omega_i, WD, (X,Y), \alpha)$ and $(\omega_i, (X,Y), \alpha)$ respectively, with ω_i being the actual rotation angle around $\vec{\omega}$. For these out-centered positions, one can wonder if the electron beam path in the ECP is still described by a circle as a given point is illuminated with different incidence conditions depending on the rotation angle.

4. Results

i. Indexation

In order to observe the influence of the scan on the indexation, it is worth considering the experimental images together with the intensity profiles extracted from different positions.

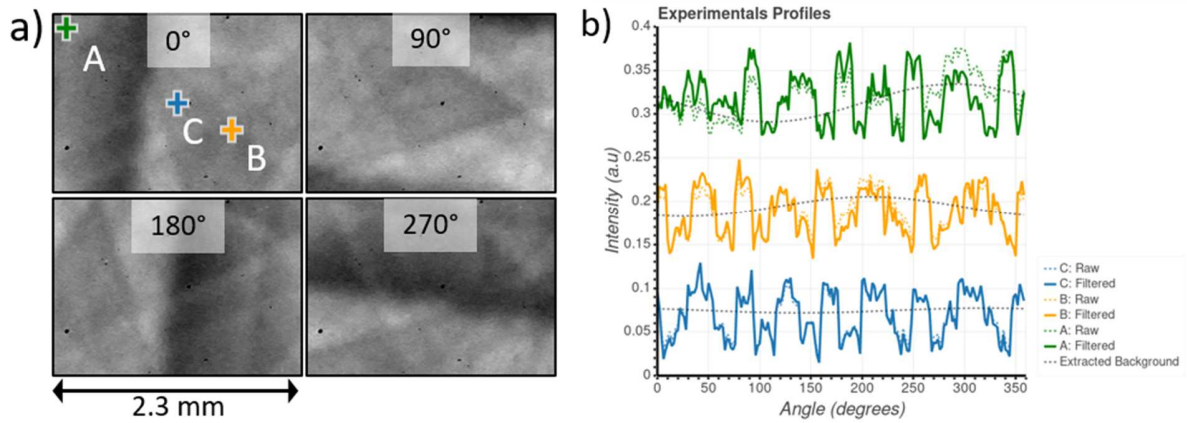

Figure 2: a) BSE images extracted from the denoised image series for different rotation angles (0°, 90°, 180°, 270°). b) Intensity profiles corresponding to three positions of the region of interest: at the center (C), at the upper left corner (A), and slightly deviated from the center (B). Raw profiles (dashed colored lines), profiles with background removed from FFT filter (lines), experimental background computed from FFT filter (black dashed lines).

As an illustrating example, Fig 2.a) presents images extracted for different angles of rotation from the image series. Fig 2.b) presents the experimental intensity profiles corresponding to three positions of the ROI: A, B, C. The raw experimental profiles are represented with colored dashed lines. The profile at the center of the ROI is considered as the reference signature of the single crystal orientation. Indeed, for this point, the beam orientation relative to the sample remains unchanged along the rotation. Point A, in the upper left, is located at a distance of 1.3 mm from the center. It corresponds to the maximum beam deflection leading to a potential impact on profiles. Point B is located at an intermediate distance of 0.5 mm from the ROI center. When comparing the profile at the center with the two other profiles, differences in position and intensity of the peaks are observed. It seems that a global intensity variation in a

wave-like form appears on the profiles, particularly visible on the profile A. This variation is considered as a background signal that is likely due to the variations, during the rotation, of both the working distance and the angle between the electron beam and the sample normal direction, which may modify the angular backscattered electron distribution on the detector. The hypothesis made is that this variation corresponds to the lowest angular frequency signal on the experimental profiles in Fourier space. In Fig 2.b), the background for each of the three experimental profiles extracted from the FFT filter are shown in black dashed lines. The background differs in shape and amplitude depending on the position relative to the center. At the center, the background is almost not present whereas a medium background is computed for point B and a more significant background concerning the A point. Filtered profiles are presented with continuous lines in Fig 2.b). The global variation is reduced for the two profiles A and B, whereas there is almost no change concerning the reference profile C. After this filtering step, the positions of the peaks are still different for profiles A and B compared to C. This indicates that the crystallographic paths followed for those two points are not the same as the one for point C.

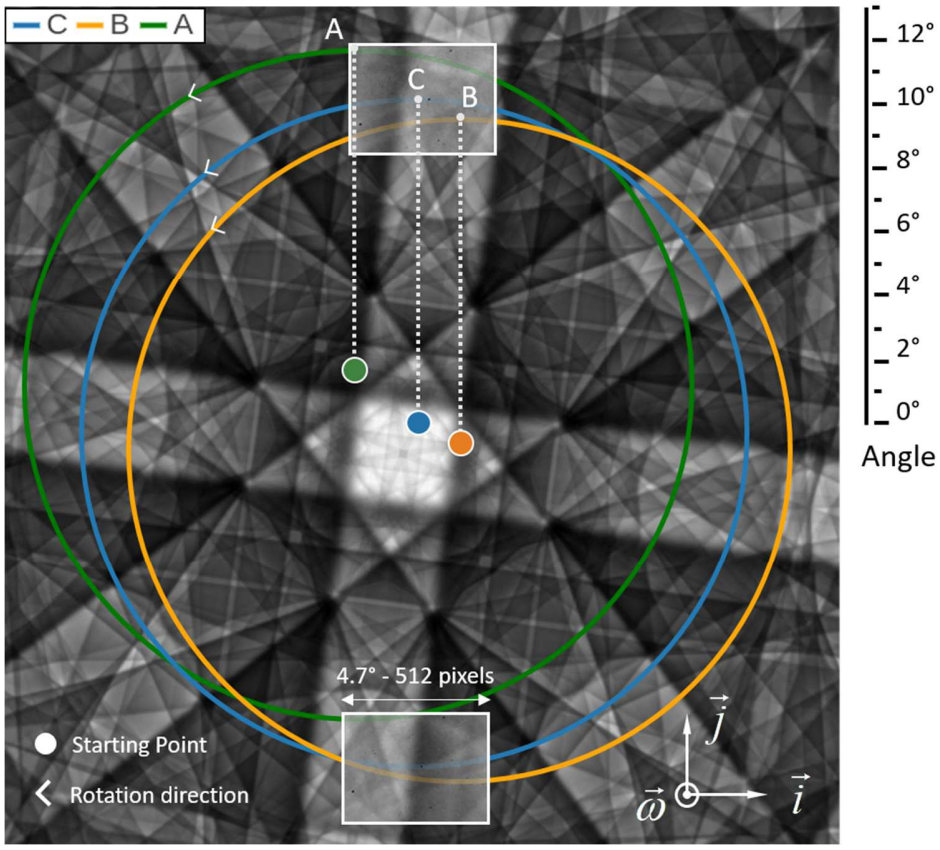

Figure 3: Simulated Electron Channeling Pattern using EMsoft [17], obtained from the Euler angles (38.77, 0.87, 85.6)° determined from profile C. Two experimental images with white square outlines are superimposed over the theoretical ECP. From the 13° known angular aperture of the theoretical ECP, an angular aperture of experimental images of 4.7° along the $\vec{i}$ axis has been determined. Circles corresponding to the three references profile A, B, C are represented using the same color code as in Figure 2.

The reference profile C is perfectly indexed from a theoretical database of 1M profiles, as there is no effect of beam deflection. An orientation of (38.77, 0.87, 85.6)° was found and the corresponding ECP was simulated. The crystallographic path corresponding to that position is a circle centered at the middle of the ECP, and with a radius of 10°. The two experimental images

of Fig 2.a) are superimposed over the simulated ECP in Fig 3. The experimental and theoretical Kikuchi bands are qualitatively fitting together, confirming the geometrical link between the experimental images and the simulated ECP. Here, the lens aberrations that certainly slightly modify the expected beam deflection are not visible due to the very small angular deflection associated to a pixel in the image, as demonstrated hereafter. This superimposition is possible due to the tilt correction carried out after the acquisition (see Appendix A): a progression of one pixel in the $\vec{x}$ direction and a progression of one pixel in the $\vec{y}$ direction at a given pixel size correspond now to the same angular deviation of the beam. This angular deviation of the beam corresponding to the progression of one pixel is designated as the "angular pixel size" (aps) in the following. A consequence is that the unknown angular pixel size of the experimental ROI is related to the simulated one of the ECP, which is known; the ECP was simulated with a 13° angular aperture. From this value, a 4.7° angular aperture of the experimental images was deduced. Knowing that the size in pixels of the ROI along the $\vec{x}$ axis corresponds to 4.7° (512 pixels), an angular pixel size of the experimental ROI of 0.01° has been estimated. It has to be noticed that this value depends on the working distance and magnification used. It is also worth noting that the beam path remains a circle for every position of the ROI. The full geometrical explanation of this assertion is provided in Appendix A. These circular beam paths for the three positions A, B, C are shown in Fig 3. Circles corresponding to beam paths A and B are centered on positions deviated from an angle compared to the ECP center, which is the center of beam path C. As a consequence, each experimental profile could be matched with theoretical profiles present in a standard database. However, a misoriention will be found compared to the reference orientation C.

To verify experimentally these assumptions, the theoretical database used for the indexation must be characterized by a mean disorientation between neighbor orientations being below 0.01°, i.e. the angular pixel size (aps). It is possible to increase the database size to obtain a mean disorientation of 0.01°, but, it would require a long time to generate and search into the database, which is not the optimal solution. The approach chosen for this specific experiment is the following: the experimental profile located at the position C (center of the ROI), is indexed using a database of 1M of theoretical profiles. Then, because the maximum disorientation in the ROI compared to the center is close to 3.0° (value calculated using the ROI dimensions in pixels and the angular pixel size), a second database of 5M is constructed and sampled around the mean orientation with a maximum disorientation of 3°. The mean disorientation between two neighbouring orientations in the resulting database is 0.01°. Fig 4.a) presents the crystalline orientation map finally obtained and Fig 4.b) shows the experimental profiles compared to the theoretical ones for the three positions A, B, C. Experimental profiles match the theoretical ones, which confirms the previous assumptions that any profiles of the ROI can be assigned with an orientation present in the database. In the next part, a procedure to correct orientations is proposed using previous assumptions.

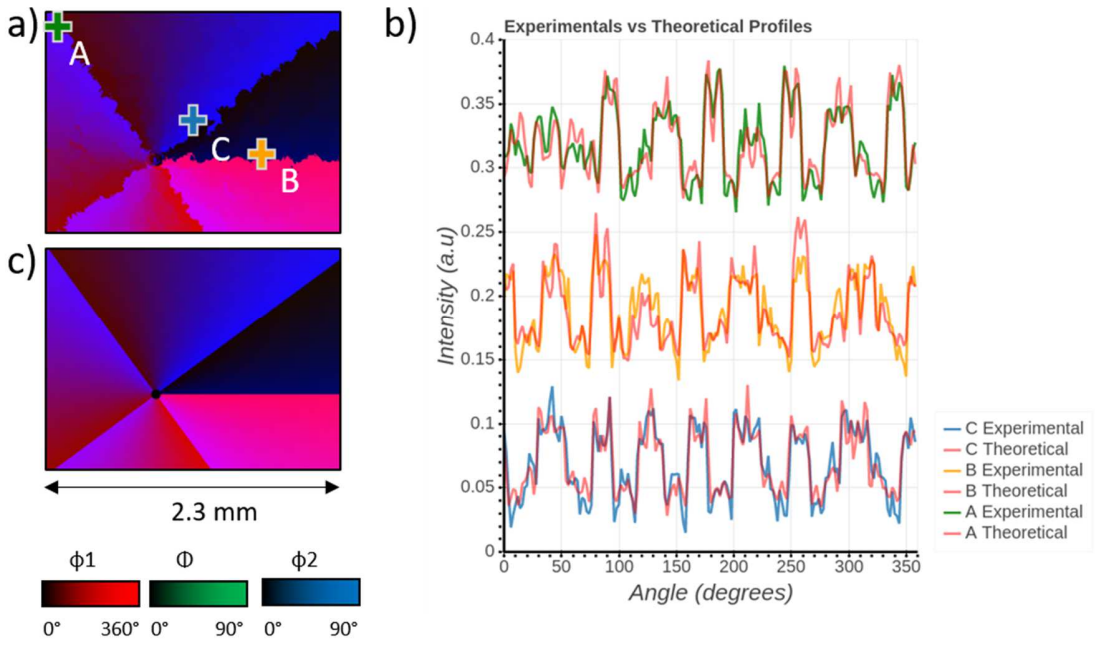

Figure 4: a) eCHORD Orientation map (Euler angles) b) Experimental versus theoretical profiles for the three reference profiles A, B, C after research in the database. c) Theoretical orientation map of the same area. Color codes corresponding to the Euler angles are indicated on the bottom of the figure.

ii. Procedure to correct orientations

The objective is to find the relation between the deviated orientations (away from the center of the field of view) and the reference orientation (at the center of the field of view). This problem can be expressed generally by multiplying the reference orientation vector with a passive rotation matrix:

$$OM_{ref} = [M_x * M_y] * OM_{misoriented} \quad (1)$$

with

$$M_x = \begin{bmatrix} 1 & 0 & 0 \\ 0 & cos(\theta_x) & -sin(\theta_x) \\ 0 & sin(\theta_x) & cos(\theta_x) \end{bmatrix}$$

$$M_y = \begin{bmatrix} cos(\theta_y) & 0 & sin(\theta_y) \\ 0 & 1 & 0 \\ -sin(\theta_y) & 0 & cos(\theta_y) \end{bmatrix}$$

The value of the angles $\theta_x$and θ_y are just the angular pixel size aps = 0.01° multiplied by coordinates X and Y (shifts from the center, expressed in pixels) of the misoriented point:

$$\begin{cases} \theta_x = X \cdot aps \\ \theta_y = Y \cdot aps \end{cases}$$

The reader can refer to the reference [18] to obtain the orientation matrix from a triplet of Euler angles. In order to confirm that the disorientations can be associated with a deviation of angle θ_x and θ_y, the theoretical expected disorientation map has been computed. For each coordinate (X, Y), matrices M_x and M_y are calculated using the respective value of θ_x and θ_y and the relation (1) is applied using as a reference the orientation (38.77, 0.87, 85.6)° found at the center of ROI. Both experimental and theoretical maps show similar gradients of Euler angles. Therefore, we can apply the correction on the experimental orientations.

iii. Corrected map

The corrected orientation map shown in Fig 5.a) has been obtained using the relation (1) for each position of the experimental orientations found on the original map on Fig 4.a). In order to confirm that the orientations computed from relation (1) are reliable, two distributions of

disorientation have been computed: the first one is obtained by comparing the orientations before the correction to the one at the ROI center, and the second by comparing the orientations after the correction to the one at the center. These two distributions are presented in the Fig 5.b). Before correction, the distribution is peaked at 1.5° with a maximum error of 3.0° whereas after correction, the distribution is peaked at 0.12°.

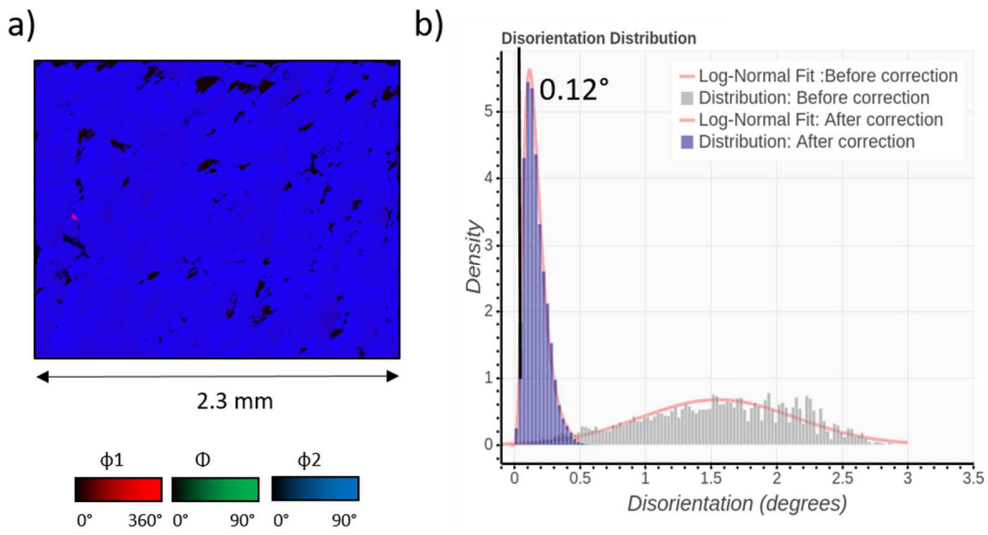

Figure 5: a) Corrected orientation map (same area as Figure4.a). Color codes corresponding to the Euler angles are indicated below the orientation map. b) Distribution of disorientations before (gray) and after (blue) correction of orientations and their corresponding log-normal fits.

5. Discussion

In the previous section, a correction procedure for orientation maps acquired for a large field of view has been presented. The peak of the misorientation distribution is shifted from 1.5° to around 0.12°. This improvement of one order of magnitude considering the size of the mapped

area is completely sufficient for most materials applications. The approach is easily extensible to polycrystal and multi-phase materials for an acquisition with the same microscope parameters. The correction matrix is only dependent on the working distance and on the pixel size. Using a single crystal, it is possible to compute the correction for different pixel sizes and working distances. However, if the distance between the pivot point P and the final objective lens (see section 1) is known, the correction matrix can be recomputed without the use of a single crystal. By comparison with the literature [14], a correction peaked at 0.09° is reachable in EBSD for a field a view of 1 mm which is in the same order of the correction obtained in eCHORD. Nevertheless, if the precision needs to be improved, it is always possible to increase the scan rate or decrease the rotation step from 2° to 1°, which would give more detailed experimental profiles. Therefore, a better similarity between experimental profiles and theoretical ones is expected and thus could improve the angular precision of the procedure if necessary.

6. Conclusion

In this paper, a method to correct the scanning beam deflection impact on eCHORD orientation maps has been proposed. It is based on a rotation matrix that corrects the orientations indexed depending on the position of the indexed profiles relative to the center of the region of interest, the working distance and the pixel size. This method has been successfully applied on a silicon single crystal with an error peaked at 0.12° over a field of view of 2.3x1.7mm^2. In the future, it would be very interesting to further decrease the magnification to reach a field of view in the centimetric range. This requires a longer working distance. For EBSD, it implies a repositioning of the EBSD detector and recalibration of the pattern center [19]. For eCHORD,

because geometrical distortions are now better understood and corrected at low magnification [20], the correction of the scan effect that we developed in this paper potentially still applies. Correcting the effect of the beam scanning paves the way to validate eCHORD as an alternative approach for simplified large area mapping.

Acknowledgements

The authors acknowledge the Centre Lyonnais de Microscopie (CLYM) for the access to the Dual-Beam FIB/SEM NVision40 microscope. MDG wishes to acknowledge funding from a DoD Vannevar-Bush Faculty Fellowship (# N00014-16-1-2821).

Appendix A: Circles in the ECP

The aim of this appendix is to demonstrate that the intensity variations for out-centered positions in the field of view can be determined by circles in the ECP computed using the intensity profiles obtained at the center of the field of view, where no beam deflection occurs due to the beam scanning. This helps to understand why out-centered intensity profiles are still present in our theoretical database of intensity profiles, but corresponding to a slightly different orientation.

The interplay between the use of a scan rotation during the acquisition and the use of the tilt correction option in the microscope is also discussed.

Reference frames

First, it is important to set up the different reference frames used in this appendix.

- The reference frame linked to the microscope itself is the direct, orthonormal one $\left(\vec{e}_x, \vec{e}_y, \vec{e}_z\right)$ defined by the tilt axis $\vec{e}_x$ of the microscope goniometer, the optical axis of the microscope column $\vec{e}_z$, pointing toward the electron gun, and $\vec{e}_y = \vec{e}_z \times \vec{e}_x$.
- Another important reference frame is the direct, orthonormal one attached to the substage. This frame $\left(\vec{i}, \vec{j}, \vec{\omega}\right)$ is defined by the rotation axis of the substage $\vec{\omega}$, and two other directions perpendicular to $\vec{\omega}$, $\vec{i}$ and $\vec{j}$, so that $\left(\vec{i}, \vec{j}, \vec{\omega}\right)$ is an orthonormal and direct frame. At the beginning of an eCHORD acquisition, the frames $\left(\vec{i}, \vec{j}, \vec{\omega}\right)$ and $\left(\vec{e}_x, \vec{e}_y, \vec{e}_z\right)$ are identical, oriented in the same way. During the acquisition, this not true anymore, and the relation between $\left(\vec{i}, \vec{j}, \vec{\omega}\right)$ and $\left(\vec{e}_x, \vec{e}_y, \vec{e}_z\right)$ will be described in the following for each step of the acquisition procedure. It is important to note that the ECP simulations are carried out in the frame $\left(\vec{i}, \vec{j}, \vec{\omega}\right)$ because this is the frame that is linked to the crystal, the sample being glued onto the substage.

Cartesian coordinates are used in these two frames.

Tilt correction and scan rotation

The experimental BSE eCHORD images are always acquired with their horizontal direction along $\vec{e}_x$ and an out-of-plane direction along the optical axis. However, if the sample is tilted around $\vec{e}_x$ by an angle α, the content of the image corresponds then to a projection of the sample surface. The spatial calibration of the image is then different along the horizontal direction and the vertical direction. To recover an identical calibration along these two directions, it is necessary

to stretch the image vertically, either by post-acquisition pixel interpolation or during the image acquisition by using the tilt correction option usually available on most of the SEM [12]. However, this tilt correction option should not be used simultaneously with the scan rotation option, because the tilt correction acts on the spacing between scan lines, which are no more parallel to the tilt axis if a scan rotation is used.

As described in the main body of the paper (see section 2. Experimental setup), the experiment used to demonstrate our correction of the beam deflection effect on the orientation map was carried out with a scan rotation to compensate for the sample rotation, in order to keep the field of view unrotated for each rotation step. In this case, the projection effect due to the tilt is digitally corrected after the acquisition. Without the scan rotation, the corners of the initial ROI would have been lost when unrotating the images and cropping them to keep the common area in all the images of the series.

On the contrary, the experiment described in this appendix has been realized with a tilt correction and no scan rotation (same single crystal, with identical microscope setup). This allows explaining more clearly the geometrical setup corresponding to the successive steps of the acquisition procedure. Only the orientation of the crystal is slightly different compared to the experiment in the body of the paper, due to a different starting point for the rotation series.

Electron Channeling Pattern geometry

One has to keep in mind that an ECP is a stereographic projection of the intensities gathered using an electron beam precessing inside a cone with a vertex located on a fixed point on the surface of the sample. Because the opening half-angle is relatively small compared to a full

stereographic projection (13° here compared to 90°), the angular deflection corresponding to a pixel in the ECP is considered as a constant all over the ECP, which is not true when considering a complete hemispherical stereographic projection, as it is visible on a Wulff net. Any pixel in the ECP is then associated to a direction of the incoming electron beam described by two angles that can be deduced from the pixel Cartesian coordinates in the frame $\left(\vec{i},\vec{j},\vec{\omega}\right)$.

In this appendix, the ECP has been simulated from the orientation obtained by using the intensity profile at the center of the field of view, where no beam deflection occurs due to the beam scan.

Why circles?

Our correction procedure relies on the fact that the intensity profiles recorded for out-centered positions still correspond to circles in the ECP computed from the orientation found at the center of the field of view (point C). Let report the acquisition geometry in this ECP Kikuchi pattern, which is computed in the $\left(\vec{i},\vec{j},\vec{\omega}\right)$ frame.

Step 1: At the beginning of the experiment, the rotation axis $\vec{\omega}$ of the substage is along $\vec{e}_z$ because the tilt around $\vec{e}_x$ is equal to 0°. As well, the rotation angle around $\vec{\omega}$ is equal to 0°. In this geometry, we have a complete correspondence between $\left(\vec{i},\vec{j},\vec{\omega}\right)$ and $\left(\vec{e}_x,\vec{e}_y,\vec{e}_z\right)$. We see Kikuchi lines in the experimental BSE image because, when scanning the ROI, the electron beam is deflected and then explore the directions around the center of the ECP. The experimental Kikuchi lines are then identical to the one visible in the center of the ECP. The horizontal and

vertical directions of the BSE image correspond to the horizontal and vertical directions in the ECP.

Step 2: The sample is tilted by an angle α around $\vec{e}_x$. In this situation, the experimental Kikuchi lines visible in the image correspond to an area in the ECP centered around a beam position inclined by an angle α in the ECP, shifted by an according number of pixels. Because $\vec{i}$ is still equal to $\vec{e}_x$ in the ECP (no rotation yet around $\vec{\omega}$), the experimental image does not need to be rotated before superimposing it on the ECP. However, $\vec{\omega}$ and $\vec{j}$ are no more parallel respectively to $\vec{e}_z$ and $\vec{e}_y$ due to the tilt. This situation is represented in Figure A.1.

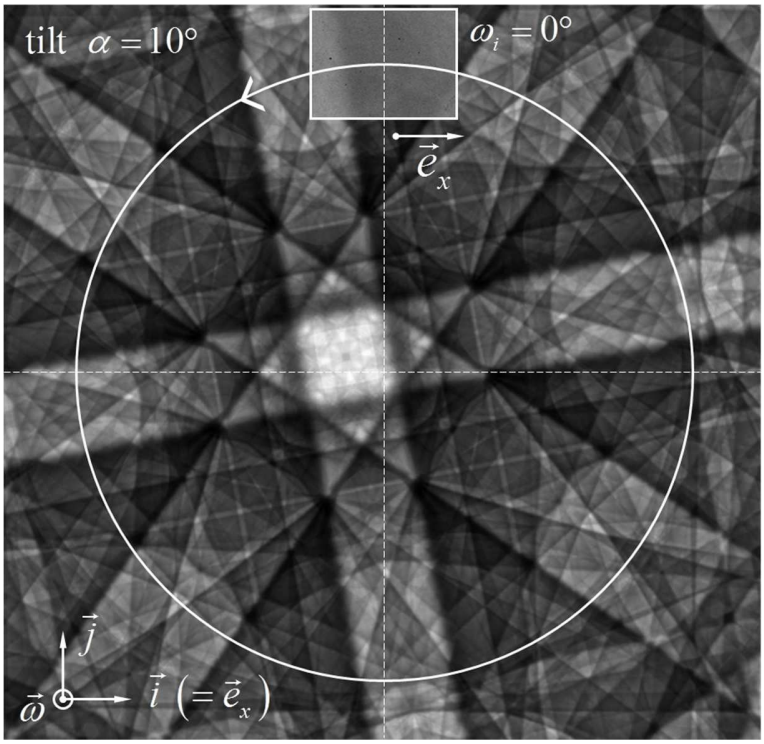

Figure A.1*: ECP simulated from the orientation deduced using the intensity profile obtained at the center of the field of view. The white circle centered in the middle of the ECP corresponds to an opening angle of* $\alpha = 10°$*. The raw experimental BSE image acquired at* $\alpha = 10°$ *but before any*

rotation is superimposed to the ECP with the center of the field of view located on the 10° circle, along $\vec{j}$.

Step 3: The sample is then rotated by an angle ω_i around $\vec{\omega}$. Because the crystal is attached to the substage that is rotated inside the microscope, the vector $\vec{e}_x$ is no more parallel to $\vec{i}$. It is still in the ECP plane $\left(\vec{i},\vec{j}\right)$, but has been rotated by an angle ω_i. Because the experimental images are always aligned with an horizontal direction along $\vec{e}_x$, they have to be rotated anti-clockwise before being superimposable onto the ECP, as demonstrated in Figure A.2..

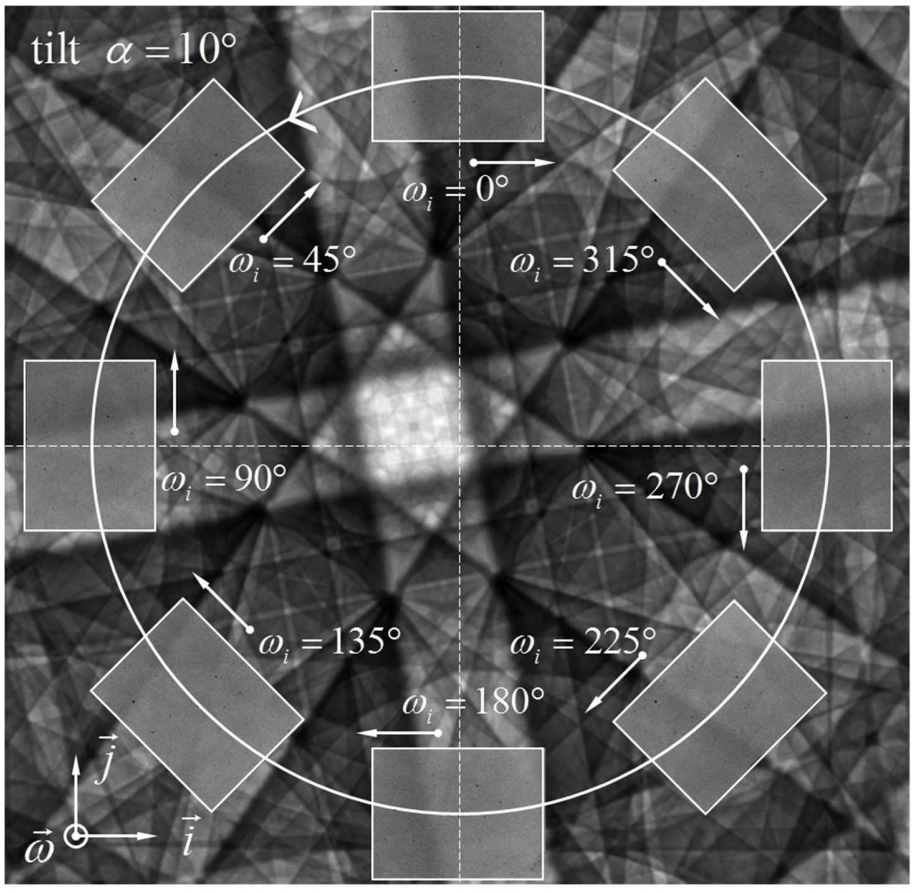

Figure A.2 : ECP with superimposed images extracted from the BSE images series. The white arrows indicate the vector $\vec{e}_x$ for the selected rotation angles around $\vec{\omega}$ indicated in the figure.

Now, let us consider the content of the raw experimental BSE images acquired at a sample tilt α around $\vec{e}_x$ and sample rotation ω_i around $\vec{\omega}$, before superimposing it on the ECP. Because $\vec{\omega}$ has been aligned with the center of the field of view during the acquisition preparation (see section 2. Experimental Set-up), the content of each image appears rotated by an angle ω_i around the center of the image compared to the situation before any rotation. When stacking all the images together, a given position on the sample surface is then rotating around the center in a clock-wise manner along the image stack depth.

On the other hand, if we stack together the images that have been anti clock-wise rotated in order to superimpose them onto the ECP, then a given position on the sample surface has fixed pixel coordinates compared to the center of the first image. Its rotation around the image center has been corrected. It means that, when considering the images superimposed on the ECP, the shift in pixels between the center of the field of view and a given position on the surface is always the same in the $\left(\vec{i}, \vec{j}, \vec{\omega}\right)$ frame, whatever the rotation angle ω_i . In other words, to go from the center of one image to a given position in the image, the same vector $\vec{V}$ has to be applied in the ECP plane, whatever the rotation. It is visible when tracking the black spots on the superimposed images as emphasized in Figure A.3.

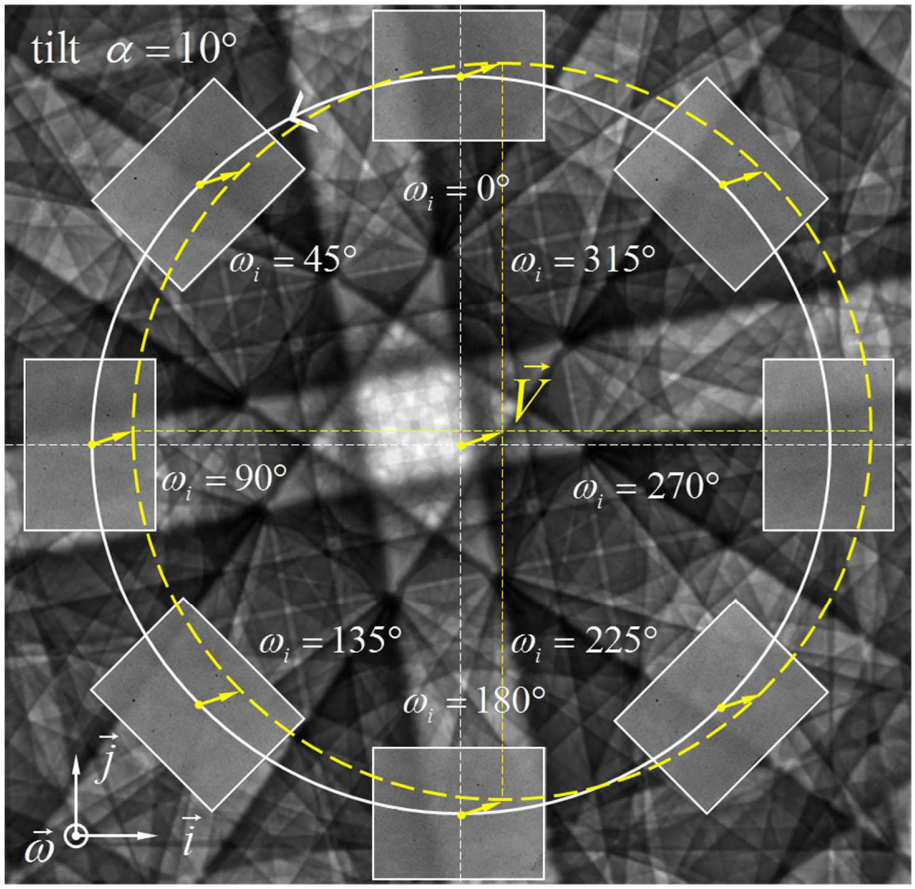

Figure A.3: ECP with superimposed images extracted from the BSE images series. The unique vector $\vec{V}$ (yellow) allowing going from the center of a given image to a given position of interest in the same image is represented for all the considered rotation angles ω_i. Because the centers of the superimposed images are all along a 10° circle, so are the positions of interest in the different images (yellow dashed circle).

In the eCHORD approach, we constitute an intensity profile for every position on the sample surface. To do this, the raw image series is aligned using the first image as a reference. This is completely equivalent to stack together all the images that has been rotated to be superimposable to the ECP. An intensity profile is then constituted by gathering the intensity

harvested at the same pixel position in all the images of the aligned stack. As evidenced in Figure A.3 (yellow dashed circle), the corresponding channeling conditions are obtained in the ECP along a circle of radius 10°, with a center shifted from the ECP center by the vector $\vec{V}$, $\vec{V}$ being the vector defined in the ECP that allows going from the center of the field of view to the position of interest. The reason is that the centers of the images are all along the white 10° circle in the ECP (centered at the middle of the ECP) and that a position of interest is always linked to the center by the same vector $\vec{V}$ whatever the rotation angle.

It is also worth noting that, if a scan rotation (without post-acquisition tilt correction) is used during the acquisition, the rotation necessary to superimpose the raw images to the ECP is already carried out, as it is the case in the experiment presented in the main body of the paper.

Conclusion of Appendix A

It is demonstrated in this appendix that the intensity profiles obtained at out-centered positions in the aligned image series corresponds to circles in the ECP computed from the intensity profile at the center of the image. These circle centers are shifted in the ECP, i.e. with centers that do not correspond to the ECP center, which simply means that they correspond to different crystallographic orientations. Our theoretical database of intensity profile being constructed by drawing circles in ECPs simulated using a sampling of the orientation space, we can conclude that even the out-centered intensity profiles are correctly described by our model.

References

[1] T. Omori, T. Kusama, S. Kawata, I. Ohnuma, Y. Sutou, Y. Araki, K. Ishida, R. Kainuma, Abnormal Grain Growth Induced by Cyclic Heat Treatment, Science. 341 (2013) 1500. doi:10.1126/science.1238017.

[2] L. Li, J.-M. Muracciole, L. Waltz, L. Sabatier, F. Barou, B. Wattrisse, Local experimental investigations of the thermomechanical behavior of a coarse-grained aluminum multicrystal using combined DIC and IRT methods, Optics and Lasers in Engineering. 81 (2016) 1–10. doi:10.1016/j.optlaseng.2016.01.001.

[3] K. Hidas, A. Tommasi, D. Mainprice, T. Chauve, F. Barou, M. Montagnat, Microstructural evolution during thermal annealing of ice-Ih, Journal of Structural Geology. 99 (2017) 31–44. doi:10.1016/j.jsg.2017.05.001.

[4] M. Bestmann, G. Pennacchioni, G. Frank, M. Göken, H. de Wall, Pseudotachylyte in muscovite-bearing quartzite: Coseismic friction-induced melting and plastic deformation of quartz, Journal of Structural Geology. 33 (2011) 169–186. doi:10.1016/j.jsg.2010.10.009.

[5] G. Nolze, Image distortions in SEM and their influences on EBSD measurements, Ultramicroscopy. 107 (2007) 172–183. doi:10.1016/j.ultramic.2006.07.003.

[6] M. Nowell, R. Anderhalt, T. Nylese, F. Eggert, R. de Kloe, M. Schleifer, S. Wright, Improved EDS Performance at EBSD Geometry, Microscopy and Microanalysis. 17 (2011) 398–399. doi:10.1017/S1431927611002868.

[7] A. Halfpenny, Some important practical issues for the collection and manipulation of Electron Backscatter Diffraction (EBSD) data from geological samples, J.Virt.Ex. 35 (2010). doi:10.3809/jvirtex.2011.00272.

[8] C. Lafond, T. Douillard, S. Cazottes, P. Steyer, C. Langlois, Electron CHanneling ORientation Determination (eCHORD): An original approach to crystalline orientation mapping, Ultramicroscopy. 186 (2018) 146–149. doi:10.1016/j.ultramic.2017.12.019.

[9] C. Langlois, T. Douillard, S. Dubail, C. Lafond, S. Cazottes, J. Silvent, A. Delobbe, P. Steyer, Angular resolution expected from iCHORD orientation maps through a revisited ion channeling model, Ultramicroscopy. 202 (2019) 68–75. doi:10.1016/j.ultramic.2019.03.007.

[10] E.F. Rauch, M. Véron, Automated crystal orientation and phase mapping in TEM, Materials Characterization. 98 (2014) 1–9. doi:10.1016/j.matchar.2014.08.010.

[11] S. Singh, M. De Graef, Dictionary Indexing of Electron Channeling Patterns, Microscopy and Microanalysis. 23 (2017) 1–10. doi:10.1017/S1431927616012769.

[12] J.I. Goldstein, D.E. Newbury, P. Echlin, D.C. Joy, C.E. Lyman, E. Lifshin, L. Sawyer, J.R. Michael, The SEM and Its Modes of Operation, in: J.I. Goldstein, D.E. Newbury, P. Echlin, D.C. Joy, C.E. Lyman, E. Lifshin, L. Sawyer, J.R. Michael (Eds.), Scanning Electron Microscopy and X-Ray Microanalysis: Third Edition, Springer US, Boston, MA, 2003: pp. 21–60. doi:10.1007/978-1-4615-0215-9_2.

[13] S.I. Wright, J.A. Basinger, M.M. Nowell, Angular Precision of Automated Electron Backscatter Diffraction Measurements, in: Materials Science Forum, 2012. doi:10.4028/www.scientific.net/MSF.702-703.548.

[14] T. Friedrich, A. Bochmann, J. Dinger, S. Teichert, Application of the pattern matching approach for EBSD calibration and orientation mapping, utilising dynamical EBSP simulations, Ultramicroscopy. 184 (2018) 44–51. doi:10.1016/j.ultramic.2017.10.006.
[15] J. Fehrenbach, P. Weiss, C. Lorenzo, Variational Algorithms to Remove Stationary Noise: Applications to Microscopy Imaging, IEEE Transactions on Image Processing. 21 (2012) 4420–4430. doi:10.1109/TIP.2012.2206037.
[16] L. Reimer, Scanning Electron Microscopy — Physics of Image Formation and Microanalysis, Springer, n.d. https://www.springer.com/gp/book/9783540639763.
[17] M. De Graef, EMsoft-org/EMsoft: Release 4.2 to synchronize with DI tutorial paper | Zenodo, (n.d.). https://zenodo.org/record/2581285#.XV-zJ3vgqbg (accessed August 23, 2019).
[18] A. Morawiec, Orientations and Rotations - Computations in Crystallographic Textures, Springer, n.d. https://www.springer.com/gp/book/9783540407348.
[19] G. Nolze, Large area EBSD mapping by single-scan technique, in: Chinese Electron Microscopy Conference, Chongqing.
[20] J.C. Weaver, W. Mershon, M. Zadrazil, M. Kooser, D. Kisailus, Wide-field SEM of semiconducting minerals, Materials Today. 13 (2010) 46–53. doi:10.1016/S1369-7021(10)70186-3.